

Pressure-Induced Amorphization and Crystallization of Heterophase Pd Nanostructures

Qian Li, Hongfei Cheng, Caihong Xing, Songhao Guo, Xiaotong Wu, Liming Zhang, Dongzhou Zhang, Xingchen Liu, Xiaodong Wen, Xujie Lü, Hua Zhang,* and Zewei Quan*

Control of structural ordering in noble metals is very important for the exploration of their properties and applications, and thus it is highly desired to have an in-depth understanding of their structural transitions. Herein, through high-pressure treatment, the mutual transformations between crystalline and amorphous phases are achieved in Pd nanosheets (NSs) and nanoparticles (NPs). The amorphous domains in the amorphous/crystalline Pd NSs exhibit pressure-induced crystallization (PIC) phenomenon, which is considered as the preferred structural response of amorphous Pd under high pressure. On the contrary, in the spherical crystalline@amorphous core-shell Pd NPs, pressure-induced amorphization (PIA) is observed in the crystalline core, in which the amorphous-crystalline phase boundary acts as the initiation site for the collapse of crystalline structure. The distinct PIC and PIA phenomena in two different heterophase Pd nanostructures might originate from the different characteristics of Pd NSs and NPs, including morphology, amorphous-crystalline interface, and lattice parameter. This work not only provides insights into the phase transition mechanisms of amorphous/crystalline heterophase noble metal nanostructures, but also offers an alternative route for engineering noble metals with different phases.

1. Introduction

Noble metal nanomaterials have demonstrated outstanding performance in broad applications, including catalysis,^[1] sensor,^[2] optics,^[3] etc., owing to their unique physicochemical properties.^[4] As known, the properties and functions of nanomaterials are greatly dependent on their atomic structures.^[5] Recently, phase engineering of nanomaterials (PEN) is emerging as a promising strategy for modulating nanomaterial properties by controlling their atomic structures.^[6] As one of the important PEN strategies, phase transformation enables the formation of nanomaterials with new phases that may not be readily prepared by conventional synthetic methods. Up to date, several phase transformation techniques, such as surface modification,^[7] high-temperature annealing,^[8] electron-beam irradiation,^[9] and high-pressure compression,^[10] have

Q. Li, X. Wu, L. Zhang, Z. Quan
Department of Chemistry
Academy for Advanced Interdisciplinary Studies
Shenzhen Engineering Research Center for Frontier Materials Synthesis
at High Pressures
Southern University of Science and Technology (SUSTech)
Shenzhen, Guangdong 518055, China
E-mail: quanzw@sustech.edu.cn

H. Cheng
Center for Programmable Materials
School of Materials Science and Engineering
Nanyang Technological University
50 Nanyang Avenue, Singapore 639798, Singapore

C. Xing, X. Liu, X. Wen
State Key Laboratory of Coal Conversion
Institute of Coal Chemistry
Chinese Academy of Sciences
Taiyuan 030001, China


S. Guo, X. Lü
Center for High Pressure Science and Technology Advanced Research
Shanghai 201203, China

D. Zhang
Partnership for Extreme Crystallography
University of Hawaii at Manoa
Honolulu, Hawaii 96822, USA

H. Zhang
Department of Chemistry
City University of Hong Kong
Hong Kong, China
E-mail: Hua.Zhang@cityu.edu.hk

H. Zhang
Hong Kong Branch of National Precious Metals Material Engineering
Research Center (NPMM)
City University of Hong Kong
Hong Kong, China

H. Zhang
Shenzhen Research Institute
City University of Hong Kong
Shenzhen 518057, China

 The ORCID identification number(s) for the author(s) of this article can be found under <https://doi.org/10.1002/smll.202106396>.

DOI: 10.1002/smll.202106396

been reported to prepare noble metal nanomaterials with new phases, including unconventional crystalline and amorphous phases.

Particularly, the static high pressure technique using diamond anvil cell offers comprehensive structure-property information during compression.^[11] Meanwhile, high pressure is able to continuously modulate material structures without changing composition, allowing for the in-situ characterization of crystal structures under compression. At high pressure, two kinds of opposite transitions can be realized, i.e., pressure-induced amorphization (PIA) and pressure-induced crystallization (PIC).^[12] The PIA refers to the structural destruction with the loss of atomic ordering, which is often observed at high pressure.^[12a,b] However, only in very few materials (e.g., metallic glass, amorphous ice, vitreous ZnCl₂),^[12c-e] the amorphous structures can be crystallized at high pressure, which normally correlates with the activation energy decrease and diffusivity variation of the materials. Systematic PIA and PIC studies could offer a deep understanding of the structural properties of order and disorder states, which are important for controlling the structural ordering and the phase engineering of materials. To the best of our knowledge, neither PIA nor PIC has been observed in noble metal nanomaterials. In this work, two kinds of heterophase Pd nanomaterials, i.e., ultrathin amorphous/crystalline Pd nanosheets (NSs)^[5c] and crystalline@amorphous core-shell Pd nanoparticles (NPs),^[5d] are used for the high-pressure study. The pressure-induced behaviors of such Pd nanomaterials are revealed to be strongly dependent on their structural characteristics, including morphology, amorphous-crystalline interface, and lattice parameter. Distinct PIC and PIA responses are observed in the heterophase Pd NSs and NPs, respectively.

2. Results and Discussion

The amorphous/crystalline heterophase Pd NSs with a thickness of ≈ 1 nm are synthesized based on the previous report,^[5d]

in which the face-centered-cubic (*fcc*) and amorphous domains are randomly distributed (Figures 1a, Figure S1 in Supporting Information). Their poor crystallinity is confirmed by the diffuse rings in the corresponding selected area electron diffraction (SAED) pattern (Figure 1a, inset). The clear lattice fringes of 1/3(422) planes with the interplanar distance of 2.36 Å in the high-resolution transmission electron microscopy (HRTEM) image (Figure 1b) and bright spots in the corresponding fast Fourier transform (FFT) pattern (Figure 1c) are observed in crystalline domains. The kinematically forbidden 1/3(422) spots are observed, which should originate from the existence of (111) twinning within the layers and the atomically thin layers.^[13] This observation is consistent with the previously reported *fcc* Pd nanosheets, suggesting that the basal plane of these Pd crystalline domains is {111}.^[13] In contrast, the amorphous domains exhibit disordered atomic arrangements in the HRTEM image (Figure 1d) and diffuse rings in the corresponding FFT pattern (Figure 1e).

In addition to the “local” atomic arrangements characterized by TEM, angle-dispersive X-ray diffraction (ADXRD) patterns provide the fingerprint of “global” structural information of these crystalline and amorphous phases. As shown in Figure 2a, these as-synthesized amorphous/crystalline heterophase Pd NSs exhibit two sets of diffraction peaks, corresponding to the crystalline phase (blue) and amorphous phase (red), respectively. The broad amorphous peak, which locates at a lower diffraction angle compared to the (111) diffraction peak, is attributed to the larger average atomic distance of disordered atomic conformation in amorphous domains.^[14] As the pressure continuously increases from 1 atm to 50.8 GPa, all the diffraction peaks in the ADXRD patterns shift towards larger diffraction angles (Figure 2a and Figure S2, Supporting Information), indicating the structural contraction of both crystalline and amorphous phases in Pd NSs.^[15] Notably, the diffraction peak of the amorphous phase gradually merges into that of the crystalline phase. Peak fitting shows that the amorphous signals become weaker and weaker above 5.0 GPa and completely disappear at 39.5 GPa. Such pressure-induced variations result in

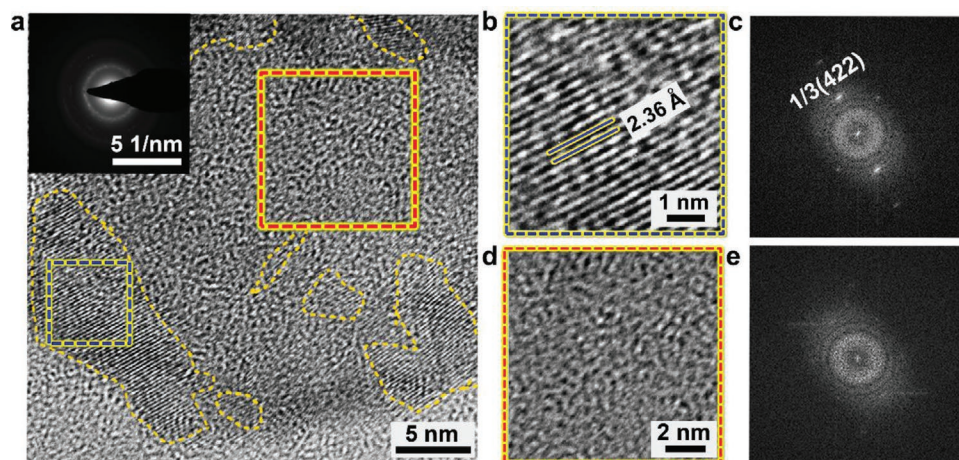


Figure 1. TEM characterizations of as-synthesized amorphous/crystalline heterophase Pd NSs before compression. a) TEM image of a representative amorphous/crystalline heterophase Pd NS. The crystalline areas are enclosed by dashed yellow curves. Inset: the corresponding SAED pattern. b) HRTEM image and c) the corresponding FFT pattern of the dashed blue square in (a). d) HRTEM image and e) the corresponding FFT pattern of the dashed red square in (a). The thickness and lateral size of the Pd NSs are ≈ 1 nm and several hundred nanometers, respectively.

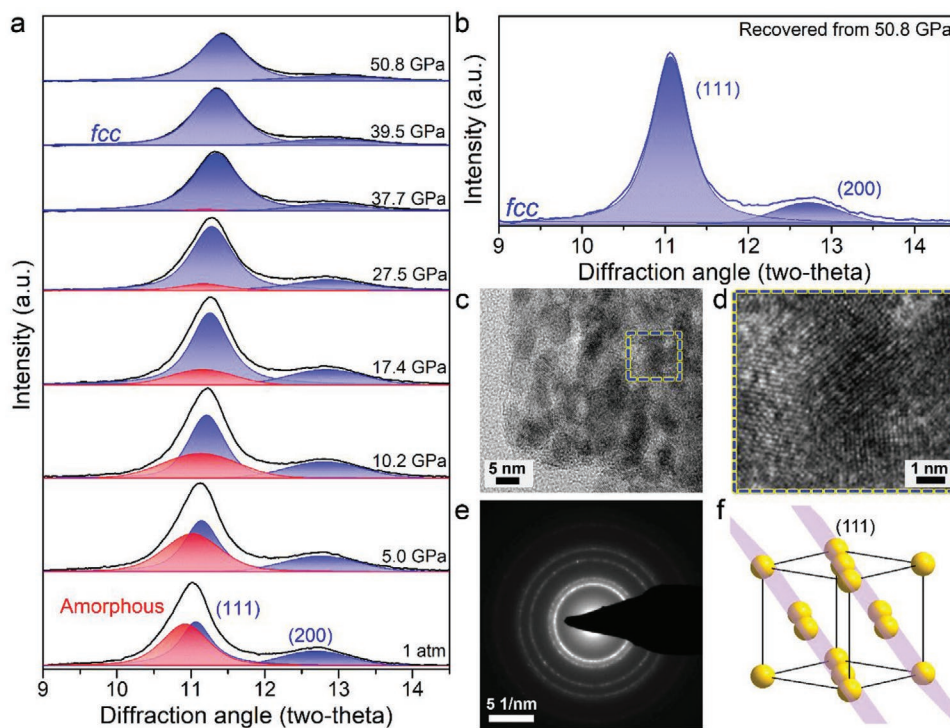


Figure 2. Ambient and high-pressure characterizations of amorphous/crystalline heterophase Pd NSs. a) Representative ADXRD patterns of the amorphous/crystalline heterophase Pd NSs under the pressure from 1 atm to 50.8 GPa. The diffraction spectra are normalized and fitted using the combined function of Lorentz and Gaussian functions. The diffraction signals of the amorphous phase and crystalline phase are shown in red and blue, respectively. b) ADXRD pattern of the recovered sample after decompression from 50.8 GPa to 1 atm. c) TEM image of the recovered Pd NSs. d) HRTEM image of the dashed blue square in (c). e) SAED pattern of the recovered Pd NSs. f) Schematic illustrations of atomic arrangements and (111) planes in Pd with *fcc* phase.

the continuously decreased peak intensity ratio of amorphous peak to crystalline (111) peak ($I_{am}/I_{(111)}$) in Figure S3, Supporting Information). Meanwhile, it indicates that structural transformation of Pd NSs from the amorphous phase to the crystalline phase, i.e., PIC, occurs between 5.0 and 39.5 GPa.

Upon releasing pressure to ambient conditions, the diffraction peaks of the crystalline phase shift back to their initial positions (Figure S4, Supporting Information), due to the decompression-induced volumetric expansion of the crystalline phase. However, only the crystalline phase is detected in the recovered ADXRD pattern, demonstrating the irreversible PIC phenomenon in Pd NSs (Figure 2b), which has also been confirmed by TEM characterizations. As shown in Figure 2c,d, the quenched Pd NSs are easy to be torn, exhibiting polycrystalline domains in which lattice fringes are arranged in random orientations. Meanwhile, the SAED pattern shows unambiguous electron diffraction rings (Figure 2e), which is indicative of the high crystallinity of the recovered sample with *fcc* structure (Figure 2f). Compared to the amorphous Pd, the higher thermodynamic stability of *fcc* phase should account for the irreversible pressure-induced phase transition in Pd NSs.^[15] Moreover, due to the two-dimensional morphology, Pd NSs are easily broken into multiple domains under compression.

Furthermore, Pd NPs with different amorphous-to-crystalline ratios are also studied, i.e., Pd NPs with pure *fcc* phase (*fcc*-Pd NPs), and crystalline@amorphous core-shell Pd NPs with lower and higher amorphous percentages, referred to as Pd NPs-L and

Pd NPs-H, respectively (Figure 3). The Pd NPs-L and Pd NPs-H are obtained through the ligand exchange of oleylamine coated on *fcc*-Pd NPs with bismuthiol I (See the experimental section in Supporting Information). As shown in Figure 3a, the amorphous signals gradually increase from *fcc*-Pd NPs to Pd NPs-H in the ADXRD patterns. Meanwhile, the ADXRD patterns show the slight structural expansions of *fcc* lattices from *fcc*-Pd NPs to crystalline@amorphous core-shell Pd NPs, which could be induced by the increased amorphization within the structures (Table S1, Supporting Information). The TEM and SAED characterizations (Figure 3b,c) indicate that the *fcc*-Pd NPs with highly crystalline structures exhibit sharp electron diffraction rings. The clear lattice fringes of (111) planes (interplanar distance of 2.33 Å) are observed (Figure 3d), showing bright spots in the corresponding FFT image (Figure 3e). The obtained crystalline@amorphous core-shell Pd NPs-L exhibits continuous lattice fringes in the core and disordered atomic arrangements in the shell (Figure 3f–h). Compared with the *fcc*-Pd NPs, a slight lattice expansion is observed in the crystalline domain of Pd NPs-L ((111) interplanar distance of 2.37 Å), which is consistent with the ADXRD result. The relatively low crystallinity of Pd NPs-L can also be confirmed with the diffuse rings and blurred spots in the corresponding SAED (Figure 3g) and FFT (Figure 3i) patterns, respectively. Compared with the *fcc*-Pd NPs and Pd NPs-L, Pd NPs-H possesses a higher percentage of the amorphous phase. Although the diffraction signal of the crystalline phase can still be detected in the ADXRD patterns

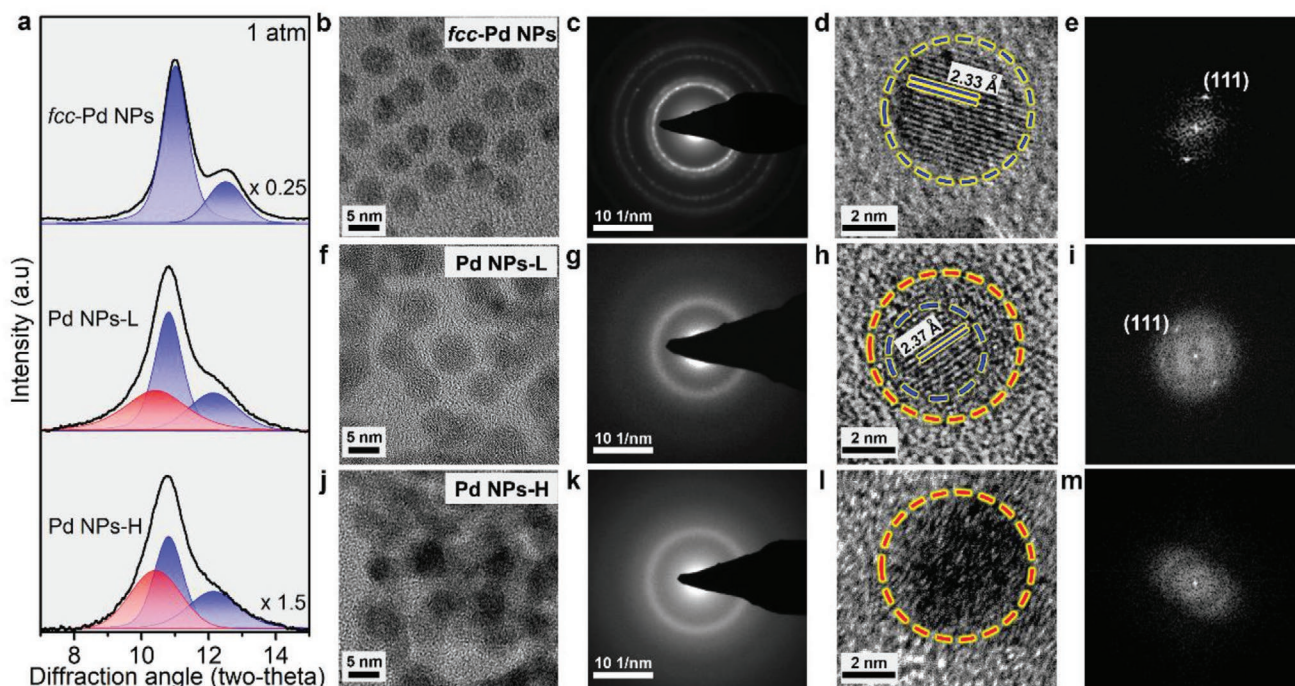


Figure 3. Ambient characterizations of as-prepared Pd NPs before compression. a) ADXRD patterns of three kinds of Pd NPs (*fcc*-Pd NPs, Pd NPs-L, and Pd NPs-H) at ambient conditions. For clarity, the intensities of diffraction signals of *fcc*-Pd NPs and Pd NPs-H are multiplied by 0.25 and 1.5, respectively. The diffraction peaks of the amorphous phase and crystalline phase are shown in red and blue, respectively. b–m) The representative TEM images (b, f, j), SAED patterns (c, g, k), HRTEM images (d, h, l), and FFT patterns (e, i, m) of *fcc*-Pd NPs (b–e), Pd NPs-L (f–i), and Pd NPs-H (j–m). The blue and red circles represent the crystalline and amorphous regions in the NPs, respectively.

(Figure 3a), it is difficult to clearly distinguish the lattice fringes in the TEM images (Figures 3j–l). The Pd atoms are observed to be randomly arranged with little periodicity, thus exhibiting blurred rings in both SAED and FFT patterns (Figures 3k–m).

High-pressure structural behaviors of these Pd NPs are deduced through their ADXRD patterns (Figure 4). The structure of *fcc*-Pd NPs keeps continuous contraction over the course of pressurization up to 50.3 GPa (Figure 4a). Through fitting the pressure-volume (P - V) data with the third-order Birch–Murnaghan equation of state, the bulk modulus (B_0) of *fcc*-Pd NPs is determined to be 291.16 GPa (Figure S5, Supporting Information). This value is much higher than the B_0 value of bulk Pd (about 190 GPa), suggesting the higher stiffness and less compressibility of *fcc*-Pd NPs during compression.^[16] A similar size effect has also been observed in Au NPs at high pressure.^[17] As for the Pd NPs-L, the continuously increased amorphous signals and decreased crystalline ones are simultaneously observed from 8.9 GPa to 47.3 GPa (Figure 4b and Figure S6, Supporting Information). The relative peak intensity ratio of crystalline phase to amorphous phase ($I_{(111)}/I_{am}$) also gradually decreases in this pressure range (Figure S7, Supporting Information). Such evolution indicates the crystalline-to-amorphous transformation, i.e., PIA, occurs in the Pd NPs-L, which is contrary to the PIC phenomenon in the amorphous/crystalline Pd NSs. In addition, the PIA response of the *fcc* cores in the crystalline@amorphous Pd NPs-L differs from the continuous contraction of *fcc*-Pd NPs, suggesting that the amorphous shell could facilitate the occurrence of PIA in the *fcc* core of Pd NPs-L. Compared to the Pd NPs-L, the Pd

NPs-H exhibits similar PIA responses (Figure 4c and Figure S8, Supporting Information). The relative peak intensity ratio of $I_{(111)}/I_{am}$ begins to decrease at 3.2 GPa and becomes zero at 26.4 GPa (Figure S9, Supporting Information). The promoted PIA process in Pd NPs-H indicates that the higher amount of amorphous shell gives rise to the lower stability of the crystalline@amorphous core-shell Pd NPs during compression.

After releasing pressure from 50.3 GPa to ambient conditions, the recovered *fcc*-Pd NPs exhibit no obvious changes in the ADXRD pattern (Figure 5a) and TEM analyses (Figure 5b–e), as compared to the original *fcc*-Pd NPs (Figures 3a–e). The observed interplanar distance of (111) remains 2.33 Å, same as the original one (Figure 3d), after releasing pressure (Figure 5d), indicating the reversible lattice contraction of the crystalline phase in *fcc*-Pd NPs under high pressure. As for the recovered Pd NPs-L, compared with the original one (Figures 3a,f,i), the enhanced diffraction signal of the amorphous phase (Figure 5a) verifies the increased percentage of amorphous structure. Meanwhile, the recovered Pd NPs-L (Figure 5f) shows diffuse rings in the SAED pattern (Figure 5g), and no clear lattice fringes (Figure 5h) or FFT spots (Figure 5i) are observed. Importantly, in the recovered Pd NPs-H, only an amorphous signal appears in the ADXRD pattern (Figure 5a), and the atomic disorder is confirmed by TEM characterization (Figures 5j–m). These results indicate that the PIA behaviors of Pd NPs-L and Pd NPs-H are irreversible after the high-pressure treatment.

Based on the aforementioned high-pressure behaviors of Pd NSs and Pd NPs, the mechanisms of their structural responses

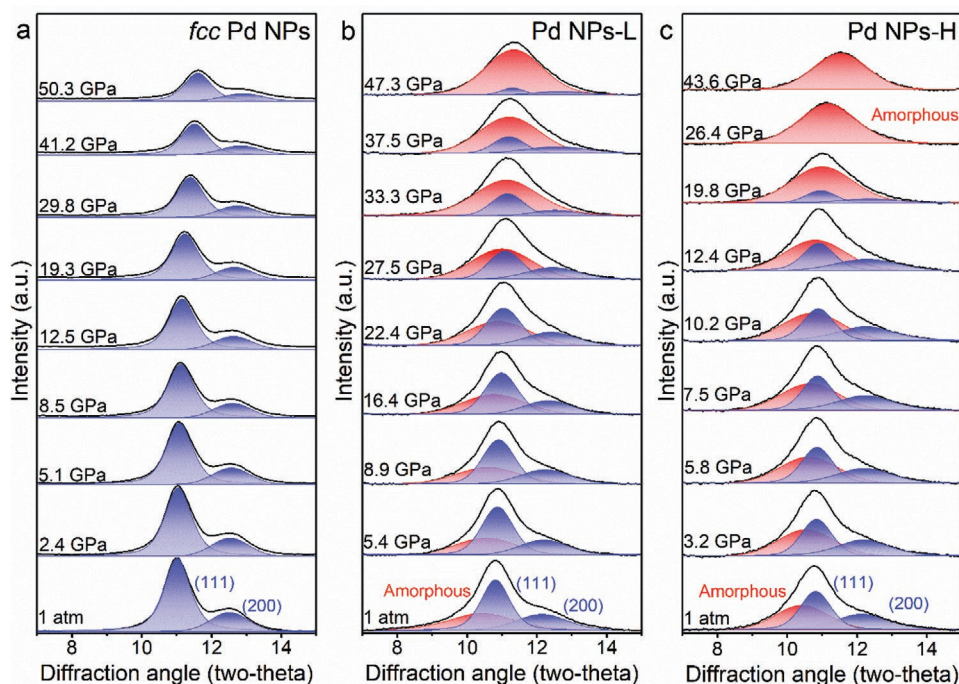


Figure 4. High pressure-induced structural evolutions of Pd NPs. a) Representative ADXR patterns of *fcc*-Pd NPs under the pressure increased from 1 atm to 50.3 GPa. b) Representative ADXR patterns of Pd NPs-L under the pressure increased from 1 atm to 47.3 GPa. c) Representative ADXR patterns of Pd NPs-H under the pressure increased from 1 atm to 43.6 GPa. The diffraction peaks highlighted with blue and red colors correspond to the diffraction signals of crystalline phase and amorphous phase in Pd NPs, respectively. The diffraction data are normalized for clarification.

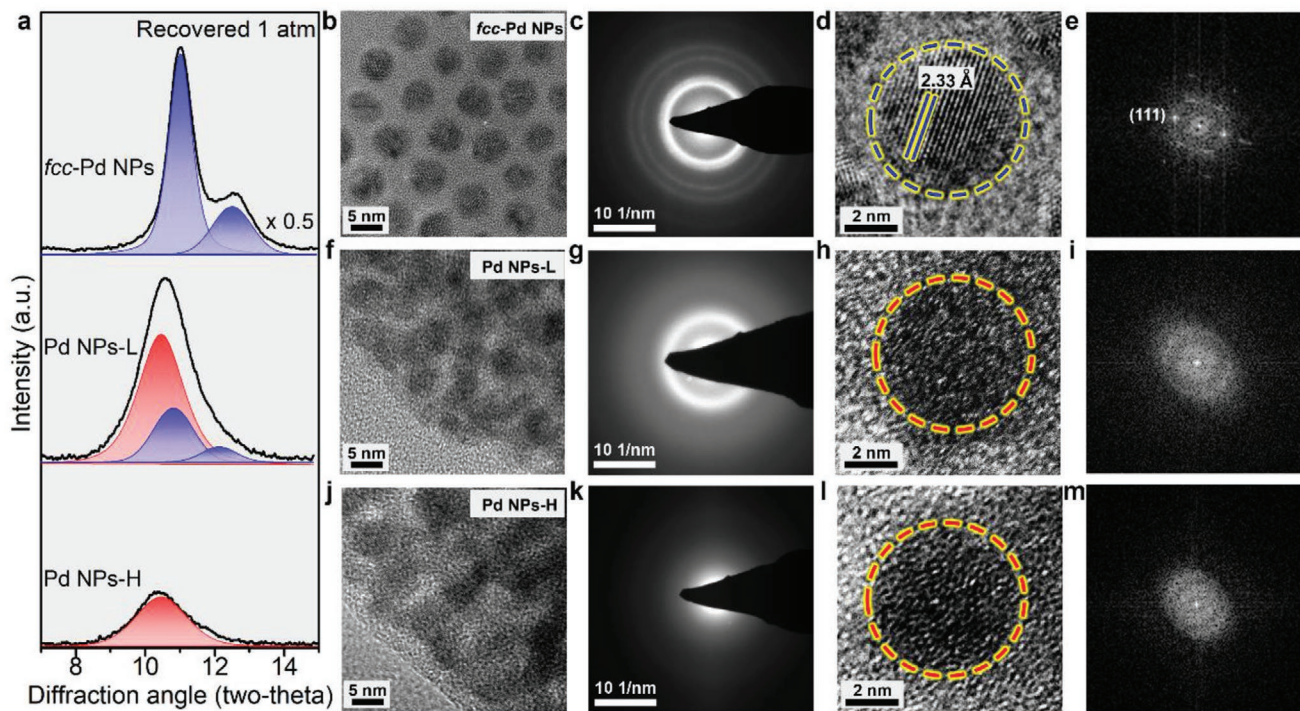


Figure 5. Structure characterizations of the recovered Pd NPs after compression. a) ADXR patterns of the recovered *fcc*-Pd NPs, Pd NPs-L, and Pd NPs-H at ambient conditions after decompressions from 50.3, 47.3, and 43.6 GPa to 1 atm, respectively. The intensity of the diffraction signal of *fcc*-Pd NPs has been multiplied by 0.5. The diffraction peaks highlighted with blue and red colors correspond to the diffraction signals of crystalline phase and amorphous phase in Pd NPs, respectively. (b–m) Representative TEM images (b, f, j), SAED patterns (c, g, k), HRTEM images (d, h, l), and FFT patterns (e, i, m) of the recovered *fcc*-Pd NPs (b–e), Pd NPs-L (f–i) and Pd NPs-H (j–m), respectively.

are proposed as follows. The *fcc* phase of Pd is thermodynamically stable at both ambient and high-pressure conditions.^[16] Upon compression, the *fcc*-Pd is stable with continuous contraction, which is confirmed by the high-pressure structural responses of the *fcc*-Pd NPs and the *fcc* domains in the amorphous/crystalline Pd NSs. As for the amorphous Pd, high entropy due to disordered atomic arrangement and unsaturated bonds in the amorphous noble metal phase makes them metastable. Hence, amorphous Pd is expected to crystallize into a stable *fcc* phase at high pressure,^[15] as evidenced by the PIC phenomenon of the amorphous domains in the amorphous/crystalline Pd NSs. However, it is worth mentioning that the structural characteristics of noble metal nanomaterials, including dimension, morphology, and interface, could affect the structural response at high pressure.^[11e] The distinct pressure-induced phase transitions in the amorphous/crystalline Pd NSs (PIC) and the crystalline@amorphous core-shell Pd NPs (PIA) can be ascribed to their different structural nature.^[18] First, high pressure is able to induce the misfit dislocations at the heterophase interfaces, resulting in the segregation of two phases along the boundaries.^[18a] The two-dimensional sheet-like morphology of Pd NSs could contribute to the pressure-induced domain separation along the amorphous-crystalline phase boundaries, as demonstrated by the multiple domains in the recovered sample (Figure 2c). In this case, the amorphous domains are expected to undergo their own structural response of PIC, which is not affected by the phase boundaries. However, in the spherical amorphous/crystalline core-shell Pd NPs, since the crystalline cores are coated by the amorphous shells, it is impossible to separate them at high pressure. The external force transfers from the outer amorphous shell to the inner crystalline core during compression, and the presence of internal heterophase interfaces in the Pd NPs are expected to affect their phase transition behavior. As the external force increases, the amorphous-crystalline interface acts as the initiation site to facilitate the phase transformation of the crystalline core.^[15,19] In addition, compared with the Pd NSs, slight lattice expansions occur in the starting amorphous/crystalline core-shell Pd NPs (Table S1, Supporting Information). The lattice expansion in nanomaterials can modify the energy of the system, soften the shear modulus and Poisson ratio, reduce the phase transition pressure, and promote the instability of the structure at high pressure.^[18c] Hence, the larger inter-planar distance of the crystalline cores in heterophase Pd NPs might also contribute to the structural collapse at high pressure. Other factors such as different surface energies and surface ligands might also affect the structural stabilities of Pd NSs and Pd NPs.^[18,19]

3. Conclusion

In summary, under high pressure, the unusual PIC and PIA phenomena are observed in the amorphous/crystalline heterophase Pd NSs and crystalline@amorphous core-shell Pd NPs, respectively. Structural responses of Pd nanostructures greatly depend on their structural characteristics. The amorphous/crystalline Pd NSs exhibit PIC response, which should be the preferred structural behavior of amorphous Pd at high pressure. In contrast, the crystalline@amorphous Pd NPs show

PIA behavior, which could be affected by the interface between the crystalline core and amorphous shell, and expanded lattice structures of the crystalline cores. This work not only gives a deep understanding of the transition between amorphous and crystalline phases in noble metals, but also provides an alternative way for phase engineering of noble metals with metastable structures, which can be used for the exploration of phase-dependent unique properties and various promising applications.

4. Experimental Section

Experimental details are provided in the Supporting Information.

Supporting Information

Supporting Information is available from the Wiley Online Library or from the author.

Acknowledgements

This work was supported by the Science and Technology Cooperation Fund between Chinese and Australian Governments (Grants 2017YFE0132300 and ACSRF65827), the National Natural Science Foundation of China (NSFC) (Grants 51772142 and 52072166), the Guangdong Science and Technology Department (Grant 2016ZT06C279), the Shenzhen Science and Technology Innovation Committee (Grant KQTD2016053019134356), the Shenzhen Engineering Research Center for Frontier Materials Synthesis at High Pressures, and the SUSTech Presidential Fund. Work performed at GSECARS (sector 13) of the Advanced Photon Source (APS) is supported by the NSF EAR-1634415 and the Department of Energy (DOE) DE-FG02-94ER14466. The APS at Argonne National Laboratory is supported by the DOE, Office of Science, under Contract No. DE-AC02-06CH11357. Experiments at Sector 13-BM-C of the APS used the PXA2 facility, supported by COMPRES under NSF Cooperative Agreement EAR-1661511. Portions of this work were carried out at the beamline 15U1, Shanghai Synchrotron Radiation Facility (SSRF). H.Z. thanks the financial support from ITC via the Hong Kong Branch of National Precious Metals Material Engineering Research Center (NPM), and the start-up grant (Project No. 9380100) and grants (Project No. 1886921) in City University of Hong Kong.

Conflict of Interest

The authors declare no conflict of interest.

Data Availability Statement

The data that support the findings of this study are available from the corresponding author upon reasonable request.

Keywords

high pressure treatment, noble metals, phase transitions, pressure-induced amorphization, pressure-induced crystallization

Received: December 23, 2021

Revised: February 20, 2022

Published online: March 28, 2022

- [1] H. Zhang, M. Jin, Y. Xiong, B. Lim, Y. Xia, *Acc. Chem. Res.* **2013**, *46*, 1783.
- [2] S. Guo, E. Wang, *Nano Today* **2011**, *6*, 240.
- [3] Y. Xia, Y. Xiong, B. Lim, S. E. Skrabalak, *Angew. Chem., Int. Ed.* **2009**, *48*, 60.
- [4] a) Q. Wei, S. Wu, Y. Sun, *Adv. Mater.* **2018**, *30*, 1802082; b) J.-Y. Kim, J. Yeom, G. Zhao, H. Calcaterra, J. Munn, P. Zhang, N. Kotov, *J. Am. Chem. Soc.* **2019**, *141*, 11739; c) S. Abalde-Cela, S. Ho, B. Rodríguez-González, M. A. Correa-Duarte, R. A. Álvarez-Puebla, L. M. Liz-Marzán, N. A. Kotov, *Angew. Chem., Int. Ed.* **2009**, *48*, 5326.
- [5] a) Z. Fan, H. Zhang, *Chem. Soc. Rev.* **2016**, *45*, 63; b) K. C. Poon, D. C. L. Tan, T. D. T. Vo, B. Khezri, H. Su, R. D. Webster, H. Sato, *J. Am. Chem. Soc.* **2014**, *136*, 5217; c) N. Yang, H. Cheng, X. Liu, Q. Yun, Y. Chen, B. Li, B. Chen, Z. Zhang, X. Chen, Q. Lu, J. Huang, Y. Huang, Y. Zong, Y. Yang, L. Gu, H. Zhang, *Adv. Mater.* **2018**, *30*, 1803234; d) H. Cheng, N. Yang, G. Liu, Y. Ge, J. Huang, Q. Yun, Y. Du, C.-J. Sun, B. Chen, J. Liu, H. Zhang, *Adv. Mater.* **2020**, *32*, 1902964.
- [6] Y. Chen, Z. Lai, X. Zhang, Z. Fan, Q. He, C. Tan, H. Zhang, *Nat. Rev. Chem.* **2020**, *4*, 243.
- [7] Z. Fan, Y. Zhu, X. Huang, Y. Han, Q. Wang, Q. Liu, Y. Huang, C. L. Gan, H. Zhang, *Angew. Chem., Int. Ed.* **2015**, *54*, 5672.
- [8] S. Sun, C. B. Murray, D. Weller, L. Folks, A. Moser, *Science* **2000**, *287*, 1989.
- [9] F. Saleem, X. Cui, Z. Zhang, Z. Liu, J. Dong, B. Chen, Y. Chen, H. Cheng, X. Zhang, F. Ding, H. Zhang, *Small* **2019**, *15*, 1903253.
- [10] a) F. Bai, K. Bian, X. Huang, Z. Wang, H. Fan, *Chem. Rev.* **2019**, *119*, 7673; b) Y. Sun, W. Yang, Y. Ren, L. Wang, C. Lei, *Small* **2011**, *7*, 606.
- [11] a) B. Li, X. Wen, R. Li, Z. Wang, P. G. Clem, H. Fan, *Nat. Commun.* **2014**, *5*, 4179; b) H. Wu, F. Bai, Z. Sun, R. E. Haddad, D. M. Boye, Z. Wang, H. Fan, *Angew. Chem., Int. Ed.* **2010**, *49*, 8431; c) H. Zhu, Y. Nagaoka, K. Hills-Kimball, R. Tan, L. Yu, Y. Fang, K. Wang, R. Li, Z. Wang, O. Chen, *J. Am. Chem. Soc.* **2017**, *139*, 8408; d) J. Lin, H. Chen, Y. Gao, Y. Cai, J. Jin, A. S. Etman, J. Kang, T. Lei, Z. Lin, M. C. Folgueras, L. N. Quan, Q. Kong, M. Sherburne, M. Asta, J. Sun, M. F. Toney, J. Wu, P. Yang, *Proc. Natl. Acad. Sci. USA* **2019**, *116*, 23404; e) Q. Guo, Y. Zhao, W. L. Mao, Z. Wang, Y. Xiong, Y. Xia, *Nano Lett.* **2008**, *8*, 972; f) S. Jiang, Y. Fang, R. Li, H. Xiao, J. Crowley, C. Wang, T. J. White, W. A. Goddard III, Z. Wang, T. Baikie, J. Fang, *Angew. Chem., Int. Ed.* **2016**, *55*, 6540; g) S. Jiang, Y. Luan, J. I. Jang, T. Baikie, X. Huang, R. Li, F. O. Saouma, Z. Wang, T. J. White, J. Fang, *J. Am. Chem. Soc.* **2018**, *140*, 13952.
- [12] a) X. Lü, Q. Hu, W. Yang, L. Bai, H. Sheng, L. Wang, F. Huang, J. Wen, D. J. Miller, Y. Zhao, *J. Am. Chem. Soc.* **2013**, *135*, 13947; b) L. Wang, W. Yang, Y. Ding, Y. Ren, S. Xiao, B. Liu, S. V. Sinogeikin, Y. Meng, D. J. Gosztola, G. Shen, R. J. Hemley, W. L. Mao, H.-k. Mao, *Phys. Rev. Lett.* **2010**, *105*, 095701; c) Q. Zeng, H. Sheng, Y. Ding, L. Wang, W. Yang, J.-Z. Jiang, W. L. Mao, H.-K. Mao, *Science* **2011**, *332*, 1404; d) R. J. Hemley, L. C. Chen, H.-K. Mao, *Nature* **1989**, *338*, 638; e) C. H. Polsky, L. M. Martinez, K. Leinenweber, M. A. VerHelst, C. A. Angell, G. H. Wolf, *Phys. Rev. B* **2000**, *61*, 5934.
- [13] a) X. Huang, S. Tang, X. Mu, Y. Dai, G. Chen, Z. Zhou, F. Ruan, Z. Yang, N. Zheng, *Nat. Nanotechnol.* **2011**, *6*, 28; b) X. Yin, X. Liu, Y.-T. Pan, K. A. Walsh, H. Yang, *Nano Lett.* **2014**, *14*, 7188.
- [14] Y. Pei, G. Zhou, N. Luan, B. Zong, M. Qiao, F. Tao, *Chem. Soc. Rev.* **2012**, *41*, 8140.
- [15] Q. Li, W. Niu, X. Liu, Y. Chen, X. Wu, X. Wen, Z. Wang, H. Zhang, Z. Quan, *J. Am. Chem. Soc.* **2018**, *140*, 15783.
- [16] Z.-L. Liu, J.-H. Yang, L.-C. Cai, F.-Q. Jing, D. Alfè, *Phys. Rev. B* **2011**, *83*, 144113.
- [17] Q. F. Gu, G. Krauss, W. Steurer, F. Gramm, A. Cervellino, *Phys. Rev. Lett.* **2008**, *100*, 045502.
- [18] a) P. Wynblatt, S. Dregia, *J. Phys. Colloques* **1990**, *51*, C1-757; b) Z. Wang, C. Schliehe, T. Wang, Y. Nagaoka, Y. C. Cao, W. A. Bassett, H. Wu, H. Fan, H. Weller, *J. Am. Chem. Soc.* **2011**, *133*, 14484; c) J. Wang, H. Zhu, C. Ma, X. Wu, J. Zhang, D. Li, R. Cong, J. Liu, Q. Cui, *J. Phys. Chem. C* **2013**, *117*, 615; d) L. Meng, J. M. D. Lane, L. Baca, J. Tafuya, T. Ao, B. Stoltzfus, M. Knudson, D. Morgan, K. Austin, C. Park, P. Chow, Y. Xiao, R. Li, Y. Qin, H. Fan, *J. Am. Chem. Soc.* **2020**, *142*, 6505.
- [19] Z. Wang, L. L. Daemen, Y. Zhao, C. S. Zha, R. T. Downs, X. Wang, Z. L. Wang, R. J. Hemley, *Nat. Mater.* **2005**, *4*, 922.